

High winter ozone pollution from carbonyl photolysis in an oil and gas basin

Peter M. Edwards^{1,2†}, Steven S. Brown¹, James M. Roberts¹, Ravan Ahmadov^{1,2}, Robert M. Banta¹, Joost A. deGouw^{1,2}, William P. Dubé^{1,2}, Robert A. Field³, James H. Flynn⁴, Jessica B. Gilman^{1,2}, Martin Graus^{1,2†}, Detlev Helmig⁵, Abigail Koss^{1,2}, Andrew O. Langford¹, Barry L. Lefer⁴, Brian M. Lerner^{1,2}, Rui Li^{1,2}, Shao-Meng Li⁶, Stuart A. McKeen^{1,2}, Shane M. Murphy³, David D. Parrish¹, Christoph J. Senff^{1,2}, Jeffrey Soltis³, Jochen Stutz⁷, Colm Sweeney^{1,2}, Chelsea R. Thompson⁵, Michael K. Trainer¹, Catalina Tsai⁷, Patrick R. Veres^{1,2}, Rebecca A. Washenfelder^{1,2}, Carsten Warneke^{1,2}, Robert J. Wild^{1,2}, Cora J. Young^{1†}, Bin Yuan^{1,2} & Robert Zamora¹

The United States is now experiencing the most rapid expansion in oil and gas production in four decades, owing in large part to implementation of new extraction technologies such as horizontal drilling combined with hydraulic fracturing. The environmental impacts of this development, from its effect on water quality¹ to the influence of increased methane leakage on climate², have been a matter of intense debate. Air quality impacts are associated with emissions of nitrogen oxides^{3,4} ($\text{NO}_x = \text{NO} + \text{NO}_2$) and volatile organic compounds⁵⁻⁷ (VOCs), whose photochemistry leads to production of ozone, a secondary pollutant with negative health effects⁸. Recent observations in oil- and gas-producing basins in the western United States have identified ozone mixing ratios well in excess of present air quality standards, but only during winter⁹⁻¹³. Understanding winter ozone production in these regions is scientifically challenging. It occurs during cold periods of snow cover when meteorological inversions concentrate air pollutants from oil and gas activities, but when solar irradiance and absolute humidity, which are both required to initiate conventional photochemistry essential for ozone production, are at a minimum. Here, using data from a remote location in the oil and gas basin of northeastern Utah and a box model, we provide a quantitative assessment of the photochemistry that leads to these extreme winter ozone pollution events, and identify key factors that control ozone production in this unique environment. We find that ozone production occurs at lower NO_x and much larger VOC concentrations than does its summertime urban counterpart, leading to carbonyl (oxygenated VOCs with a C=O moiety) photolysis as a dominant oxidant source. Extreme VOC concentrations optimize the ozone production efficiency of NO_x . There is considerable potential for global growth in oil and gas extraction from shale. This analysis could help inform strategies to monitor and mitigate air quality impacts and provide broader insight into the response of winter ozone to primary pollutants.

One of the key scientific challenges in understanding winter ozone (O_3) is determining the source of the radicals (gas-phase molecules with an unpaired electron that react rapidly with VOCs) required to initiate and sustain oxidation cycles. Quantifying these sources is essential for understanding the individual roles of NO_x and VOCs during these O_3 pollution episodes and for the design of mitigation strategies^{9,14}. By far the largest radical source in the lower atmosphere is the photolysis of O_3 itself, which produces a small yield of electronically excited oxygen atoms, $\text{O}(^1\text{D})$, some of which react with water vapour to produce hydroxyl (OH) radicals¹⁵. During mid-latitude winter, both ultraviolet light and, especially, water vapour are far less abundant than in summer, leading to a 15- to 60-fold decrease in primary OH production through this

mechanism^{16,17}. The seasonal cycle in mid-latitude OH production is responsible for the summertime maxima in urban O_3 but presents a conundrum for understanding winter O_3 events (Fig. 1).

The Uintah Basin Winter Ozone Studies (UBWOS) were a set of field intensives (large sets of air and radiation measurements occurring for a limited duration, typically weeks to months) at a remote location (40.1437° N, 109.4680° W) within the oil and gas basin of northeastern Utah (Fig. 1) during January and February of 2012, 2013 and 2014, motivated by observations of high O_3 in two preceding years. Winter O_3 is

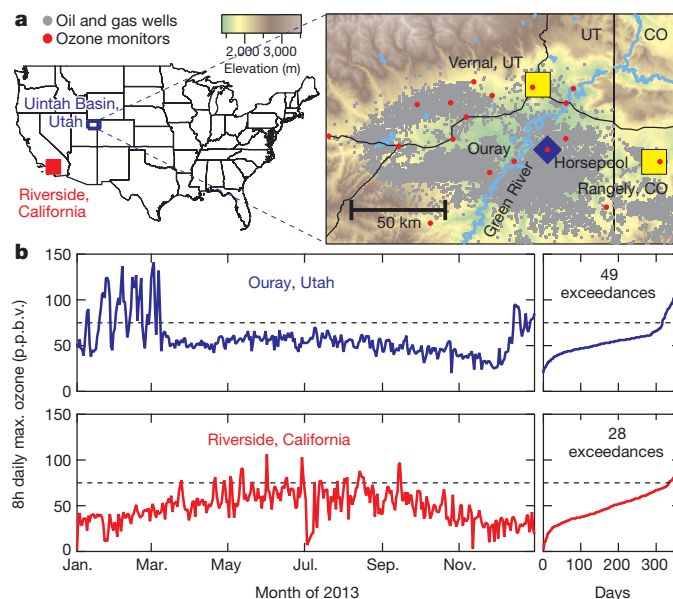


Figure 1 | Seasonal cycle of O_3 in the Uintah Basin, Utah and the Los Angeles Basin, California in 2013. **a**, Digital elevation map (elevation indicated by colour scale) of the Uintah Basin showing oil and gas wells (grey dots), O_3 monitors (red circles) urban centres (yellow squares) and the site of the field intensives (Horsepool, blue diamond). **b**, Graphs at left show daily maximum 8-h average O_3 for 2013 at Ouray, Utah, a remote site in the Uintah Basin (population 50,000), and Riverside, California, an urban receptor site in the eastern Los Angeles Basin, a region with 18 million residents. Graphs at right show data sorted by increasing O_3 mixing ratio, together with the number of days in excess of the US national ambient air quality standard (75 p.p.b.v., 8 h average; black dashed line). In 2013, O_3 exceedances were more frequent and greater in severity at Ouray than at Riverside, despite the large difference in population.

¹NOAA Earth System Research Laboratory, Boulder, Colorado 80305, USA. ²Cooperative Institute for Research in Environmental Sciences, University of Colorado, Boulder, Colorado 80309, USA.

³Department of Atmospheric Science, University of Wyoming, Laramie, Wyoming 82070, USA. ⁴Department of Earth and Atmospheric Sciences, University of Houston, Houston, Texas 77204, USA. ⁵Institute of Arctic and Alpine Research, University of Colorado, Boulder, Colorado 80309, USA. ⁶Air Quality Research Division, Environment Canada, Toronto, Ontario M3H 5T4, Canada. ⁷Department of Oceanic and Atmospheric Sciences, University of California, Los Angeles, Los Angeles, California 90095, USA. [†]Present addresses: Department of Chemistry, University of York, York YO10 5DD, UK (P.M.E.); Institute of Meteorology and Geophysics, University of Innsbruck, Innsbruck, 6020 Austria (M.G.); Department of Chemistry, Memorial University of Newfoundland, St John's, Newfoundland A1B 3X7, Canada (C.J.Y.).

clearly related to oil and gas emissions; although inventories remain uncertain, the US Environmental Protection Agency estimates that oil and gas activities are responsible for 62% of NO_x emissions and 97% of VOC emissions in the two counties that comprise the Utah side of the basin. The winter of 2011–2012 was warm, with no snow cover and only moderate (16 p.p.b. d^{-1} average) O_3 production and no O_3 in excess of 51 p.p.b. by volume¹⁶ (p.p.b.v.). Multiple strong O_3 events occurred during the colder and consistently snow covered winter of 2012–13, with threefold-greater daily average O_3 production than during the previous year. Meteorologically stagnant conditions that concentrate emissions in a shallow boundary layer have been a prerequisite of winter O_3 events observed thus far. These conditions are amenable to treatment with a box model, in which the relevant chemical reactions are simulated in a zero-dimensional ‘box’; emissions of primary pollutants into the box are included, and transport and dry deposition processes are represented through a first-order loss term. Further details of the model, containing an updated Master Chemical Mechanism v3.2 chemistry scheme¹⁸ containing more than 10,000 reactions, is in Methods. The near-explicit model of radical sources, propagation and amplification allows a powerful analysis of the factors that govern winter O_3 production and that differentiate it from its summer, urban counterpart.

Figure 2 shows a single, stagnant, 6 d period (31st January to 5th February 2013) during which daily-mean O_3 mixing ratios increased from 54 to 95 p.p.b.v. and the daily maximum 8 h-average O_3 increased from 67 to 107 p.p.b.v. This event was the longest sustained build-up of O_3 , although even higher mixing ratios were observed during the 2013 study (Fig. 1). Throughout this period, the model reproduces the observed build-up and diurnal cycle of O_3 , with a mean 10 min-average model-to-measurement discrepancy of $+4\%$. The model also accurately reproduces observed concentrations of the key oxidized reactive nitrogen (for example peroxyacetyl nitrate, with an average model deviation of $+1\%$) and oxygenated VOCs (for example acetaldehyde, -2%) over the 6 d simulation, providing additional confidence in the simulation of VOC- NO_x photochemistry and O_3 production. Further details on model performance are in Methods.

The detailed chemical mechanism enables the identification of the radical sources that drive O_3 production. The pie charts on the right

side of Fig. 2 and Extended Data Table 3 show the integrated radical sources on the final day of the simulation. Primary OH production through $\text{O}(^1\text{D}) + \text{H}_2\text{O}$ was small ($0.74 \text{ p.p.b.v. d}^{-1}$, or 4% of the total), as is expected for this winter environment. By comparison, this source is approximately $10 \text{ p.p.b.v. d}^{-1}$ in the Los Angeles basin in summer¹⁹, but was only $0.17 \text{ p.p.b.v. d}^{-1}$ during UBWOS 2012, when O_3 levels were much lower¹⁶. The reaction of O_3 with unsaturated hydrocarbons (alkenes) is an OH source that can be large during periods of high urban O_3 (ref. 20), but contributes only $0.34 \text{ p.p.b.v. d}^{-1}$ (1.8% of the total) here owing to the low emissions of alkenes relative to alkanes and aromatics⁵. Photolysis of nitryl chloride, ClNO_2 , which arises from the night-time heterogeneous reactions of nitrogen oxides²¹ was also small, probably as a result of a lack of aerosol-phase chloride. Nitrous acid (HNO_2) also forms from heterogeneous reactions of nitrogen oxides, and photolyses readily to produce OH radicals. The sources and atmospheric chemistry of HNO_2 have been the subject of intense recent interest (see, for example, ref. 22), including during the winter of 2011 in Wyoming¹². The photolysis of HNO_2 was the least certain free-radical source because of the difficulty in measuring it reliably. The HNO_2 contribution to UBWOS 2013 in Fig. 2 is an estimate based on measurements in 2012 (Methods). The shaded region in the plot of O_3 in Fig. 2 illustrates the effect of HNO_2 on the calculated O_3 , with the lower bound being a simulation with zero HNO_2 and the upper bound a simulation with a twofold increase in HNO_2 . This radical source is not required to simulate O_3 build-up events accurately, although it may have a significant role during the initiation stages, when other radical sources are smaller.

By far the dominant radical source (85%) in the simulation on day six is the photolysis of carbonyl compounds. The model under-predicted formaldehyde, the simplest carbonyl, by 30%, and an additional constant formaldehyde source was added to achieve agreement with observations. This source could arise from a direct emission or incomplete model chemistry. Removal of this source results in 6%-lower peak O_3 on day six. Even with additional formaldehyde added to the model, the majority of the radical production on day six ($9.3 \text{ p.p.b.v. d}^{-1}$ and 50.5%) is due to the photolysis of larger carbonyl compounds (keto-aldehydes, glyoxal + methyl glyoxal and mono-aldehydes, comprising 13.5, 11.2 and 9.3%, respectively). Although carbonyl compounds are products of VOC oxidation,

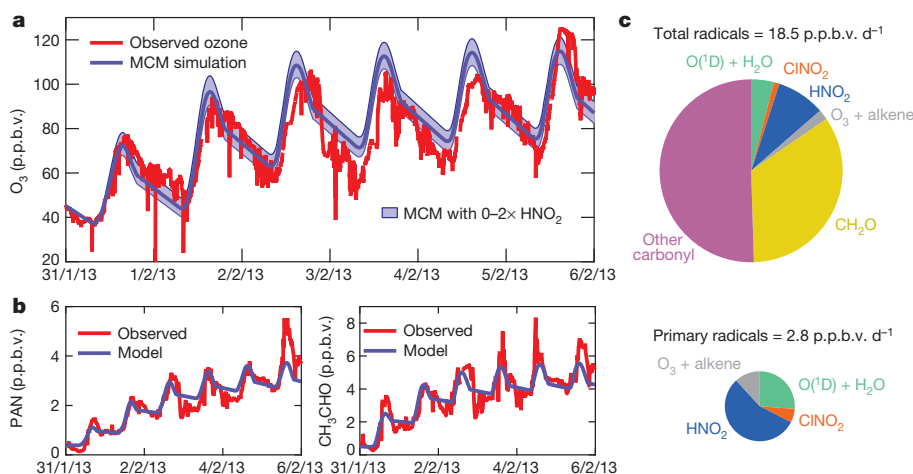


Figure 2 | Observed and modelled photochemistry at Horsepool, Utah.

a, Observed ozone (red) during a multi-day meteorological stagnation event. Overlaid on the observations is a chemical box model simulation (blue) employing the Master Chemical Mechanism scheme. The solid line is the base simulation (see main text and Methods), and the shaded region is the range of simulation without photolysis of nitrous acid (HNO_2) or with twice the base-case HNO_2 photolysis as a radical source. **b**, Comparison between model (blue) and measurement (red) for peroxyacetyl nitrate (PAN; left) and acetaldehyde (CH_3CHO ; right), which are the photochemical oxidation products of reactive nitrogen and VOCs, respectively. **c**, Contributions of different free radical sources on day six of the simulation for total sources (top)

and primary sources only (bottom), sized according to their relative magnitudes. The lower pie chart illustrates only the primary radical production (O_3 photolysis, O_3 alkene reactions and photolysis of radical precursors produced in heterogeneous nitrogen oxide reactions). If the additional 30% H_2CO added to the model arises from an emission source, it would represent a primary radical source and would be included in the lower pie chart. These sources are presumably responsible for initiation of the early stages of O_3 production. O_3 photolysis and reaction with alkenes, which are shown for day six of the simulation, scale with O_3 itself and are therefore smaller contributors at the onset of O_3 build-up events.

they are net radical sources that function as radical amplifiers because they are chemically stable products formed during radical propagation chains (that is, reactions that consume and produce one radical). Further details on this process are in Methods.

As noted above, no high- O_3 events occurred during the 2012 study, raising the question of the role of snow cover in driving O_3 production. The principal effects of snow cover are to increase surface albedo and, thus, actinic flux for photolysis reactions, and to reduce the mixed-layer height, concentrating primary emissions. Simulations with reduced albedo (from the observed 0.85 to 0.1) but the same emissions and physical loss of NO_x and VOC result in a 33% decrease in peak O_3 on day six. A simulation with VOC mixing ratios equivalent to those of the 2012 study year (that is, assuming the same high VOC emissions between the two years, but with greater dilution in 2012), but with an albedo of 0.85, results in a 45% reduction in peak O_3 on day six¹⁶. Thus, both high VOC emissions into a shallow, stable boundary layer, and increased photolysis rates due to the snow albedo, are required for rapid winter O_3 production.

A key question in the design of O_3 mitigation strategies is the relative effectiveness of emissions reductions in VOC precursors versus NO_x precursors¹⁴. Analysis of the lower- O_3 year during UBWOS 2012 showed it to be radical limited¹⁶, because the rate of radical production was small compared with the rate of emission of NO_x (ref. 23), which determines the rate of radical removal. Radical limitation normally leads to NO_x saturation (that is, increased NO_x leads to decreased O_3), which is typical of most urban areas in winter, where O_3 is generally well below air quality standards. Figure 3 shows the contours of an O_3 isopleth diagram for the build-up event in Fig. 2, that is, peak O_3 on day six of the simulation as a function of NO_x and VOC emissions, normalized to unity for the base-case simulation of Fig. 2. The total net radical production of 18.5 p.p.b.v. d^{-1} is sufficient to prevent NO_x saturation. As the right-most graphs in Fig. 3 show, NO_x is near its peak efficiency for O_3 production, and the response of O_3 to VOC emissions is just beyond the transition from VOC sensitive to VOC saturated. These results contrast with an earlier model study of the Upper Green River Basin, Wyoming, in which simulations of three of four events were NO_x saturated and VOC sensitive according to analysis of single-day events using a lumped VOC degradation scheme⁹.

The isopleth diagram in Fig. 3 appears similar to that for summer urban O_3 (ref. 14). However, the graphs on the left-hand side of the figure, which compare NO_x , VOC mixing ratios and OH reactivity

(see below) in the Uintah Basin in winter to the Los Angeles Basin in early summer (May–June), illustrate significant differences. The Los Angeles measurements are from the CalNex field intensive (May–June 2010, Pasadena, California), during which the maximum 8 h-average O_3 reached 84 p.p.b.v. The distributions of NO_x and VOCs in these environments are quite different, with much (nearly fourfold) lower NO_x but much (~15 times) greater VOC in the Uintah Basin. The composition of VOCs from urban emissions differs considerably from that of VOCs from oil- and gas-producing regions⁵, with the latter dominated by compounds (that is, light alkanes) that are less reactive to OH radicals and, thus, less effective at producing O_3 (ref. 24). Even accounting for this difference, the median calculated OH reactivity (that is, the sum of all VOC + OH rate coefficients multiplied by the VOC concentration) is 4.6 times greater in the Uintah Basin than in Los Angeles. (We note that methane, although abundant in the Uintah Basin²⁵, accounts for less than 1.5% of the calculated OH reactivity.) Thus, although similar in appearance to that of an urban area, the O_3 isopleth in Fig. 3 occupies a very different NO_x –VOC space. Were NO_x in the wintertime Uintah Basin more comparable to that of urban settings historically, the O_3 photochemistry would be fully NO_x saturated and O_3 production would thus be significantly less efficient. Conversely, if the VOC mixing ratios and OH reactivity in the wintertime Uintah Basin were more typical of an urban area, the photochemistry would not give rise to strong O_3 events. It is the exceedingly high VOC concentrations, and the radicals produced during their oxidation, in the oil and gas region that leads to highly efficient O_3 production.

Although observed extreme winter O_3 events in the United States have been limited to meteorologically stagnant conditions in mountain basins, similar phenomena may occur in regions with oil and gas development without routine air quality monitoring¹³. Present emissions trends in the United States are towards lower NO_x from urban and power generation sources^{26,27}, and increasing methane and VOCs from fossil fuel development⁷. Urban areas in close proximity to oil- and gas-producing regions may tend towards more efficient O_3 production during the winter season, with as yet unrecognized consequences. Shale gas development in other mid- or high-latitude regions that may experience stable winter meteorology, such as continental Europe²⁸, the United Kingdom²⁹ and China³⁰ lags that of the United States but holds the same potential for rapid exploitation³¹. The measurement and model framework outlined here will serve to better define emerging air quality issues associated with global development of new fossil fuel resources.

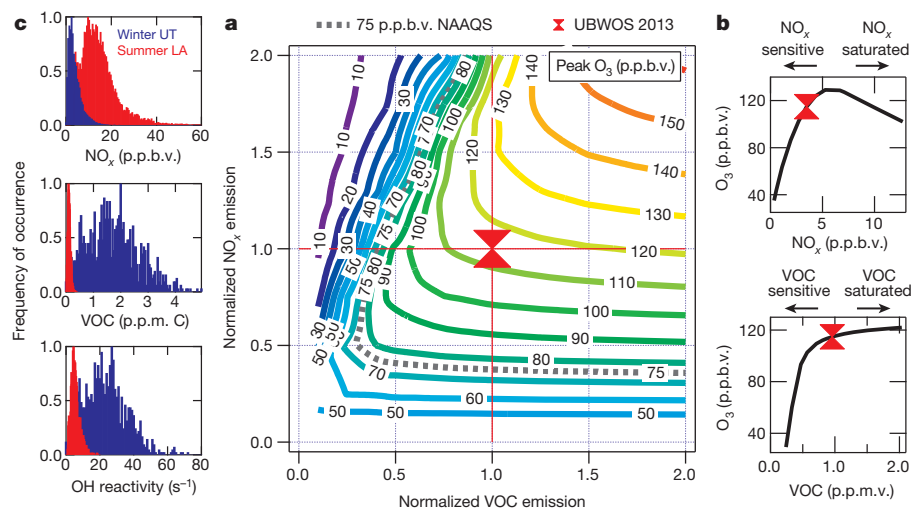


Figure 3 | Isopleth diagram for winter O_3 production. **a**, Isopleth with contours showing peak O_3 on day six of the simulation in Fig. 2 as a function of the emissions of NO_x and VOC in the model relative to the base case (red symbol). The dashed line indicates the 75 p.p.b.v. US national ambient air quality standard (NAAQS). **b**, Response of peak O_3 to NO_x (top) and VOC (bottom), expressed in mixing ratio units. These plots are slices through the

surface at the red horizontal and vertical lines in the isopleth diagram, with the base case shown as the red symbol. **c**, Comparison of distributions of NO_x (top), VOC (middle, expressed as parts per million carbon) and calculated OH reactivity with respect to VOC (bottom; see text) for the Uintah Basin, Utah in January–February 2013 (blue bars) and for measurements in May–June 2010 in Pasadena, California in the Los Angeles Basin (red bars).

Online Content Methods, along with any additional Extended Data display items and Source Data, are available in the online version of the paper; references unique to these sections appear only in the online paper.

Received 15 May; accepted 6 August 2014.

Published online 1 October; corrected online 15 October 2014 (see full-text HTML version for details).

- Li, H. & Carlson, K. H. Distribution and origin of groundwater methane in the Wattenberg oil and gas field of northern Colorado. *Environ. Sci. Technol.* **48**, 1484–1491 (2014).
- Brandt, A. R. *et al.* Methane leaks from North American natural gas systems. *Science* **343**, 733–735 (2014).
- McLinden, C. A. *et al.* Air quality over the Canadian oil sands: a first assessment using satellite observations. *Geophys. Res. Lett.* **39**, L04804 (2012).
- Carlton, A. G., Little, E., Moeller, M., Odoyo, S. & Shepson, P. B. The data gap: can a lack of monitors obscure loss of clean air act benefits in fracking areas? *Environ. Sci. Technol.* **48**, 893–894 (2014).
- Gilman, J. B., Lerner, B. M., Kuster, W. C. & de Gouw, J. A. Source signature of volatile organic compounds from oil and natural gas operations in northeastern Colorado. *Environ. Sci. Technol.* **47**, 1297–1305 (2013).
- Katzenstein, A. S., Doezema, L. A., Simpson, I. J., Blake, D. R. & Rowland, F. S. Extensive regional atmospheric hydrocarbon pollution in the southwestern United States. *Proc. Natl Acad. Sci. USA* **100**, 11975–11979 (2003).
- Pétron, G. *et al.* Hydrocarbon emissions characterization in the Colorado Front Range: a pilot study. *J. Geophys. Res.* **117**, D04304 (2012).
- Jerrett, M. *et al.* Long-term ozone exposure and mortality. *N. Engl. J. Med.* **360**, 1085–1095 (2009).
- Carter, W. P. L. & Seinfeld, J. H. Winter ozone formation and VOC incremental reactivities in the Upper Green River Basin of Wyoming. *Atmos. Environ.* **50**, 255–266 (2012).
- Helmig, D., Thompson, C., Evans, J. & Park, J.-H. Highly elevated atmospheric levels of volatile organic compounds in the Uintah Basin, Utah. *Environ. Sci. Technol.* **48**, 4707–4715 (2014).
- Oltmans, S. *et al.* Anatomy of wintertime ozone associated with oil and natural gas extraction activity in Wyoming and Utah. *Elem. Sci. Anth.* **2**, 000024 (2014).
- Rappenglück, B. *et al.* Strong wintertime ozone events in the Upper Green River Basin, Wyoming. *Atmos. Chem. Phys.* **14**, 4909–4934 (2014).
- Schnell, R. C. *et al.* Rapid photochemical production of ozone at high concentrations in a rural site during winter. *Nature Geosci.* **2**, 120–122 (2009).
- Seinfeld, J. H. Urban air pollution: state of the science. *Science* **243**, 745–752 (1989).
- Levy, H. Normal atmosphere: large radical and formaldehyde concentrations predicted. *Science* **173**, 141–143 (1971).
- Edwards, P. M. *et al.* Ozone photochemistry in an oil and natural gas extraction region during winter: simulations of a snow-free season in the Uintah Basin, Utah. *Atmos. Chem. Phys.* **13**, 8955–8971 (2013).
- Heard, D. E. *et al.* High levels of the hydroxyl radical in the winter urban troposphere. *Geophys. Res. Lett.* **31**, L18112 (2004).
- Jenkin, M. E., Saunders, S. M. & Pilling, M. J. The tropospheric degradation of volatile organic compounds: a protocol for mechanism development. *Atmos. Environ.* **31**, 81–104 (1997).
- Young, C. J. *et al.* Vertically resolved measurements of nighttime radical reservoirs in Los Angeles and their contribution to the urban radical budget. *Environ. Sci. Technol.* **46**, 10965–10973 (2012).
- Paulson, S. E. & Orlando, J. J. The reactions of ozone with alkenes: an important source of HO_x in the boundary layer. *Geophys. Res. Lett.* **23**, 3727–3730 (1996).
- Thornton, J. A. *et al.* A large atomic chlorine source inferred from mid-continental reactive nitrogen chemistry. *Nature* **464**, 271–274 (2010).
- Li, X. *et al.* Missing gas-phase source of HONO inferred from zeppelin measurements in the troposphere. *Science* **344**, 292–296 (2014).
- Kleinman, L. I. The dependence of tropospheric ozone production rate on ozone precursors. *Atmos. Environ.* **39**, 575–586 (2005).
- Russell, A. *et al.* Urban ozone control and atmospheric reactivity of organic gases. *Science* **269**, 491–495 (1995).
- Karion, A. *et al.* Methane emissions estimate from airborne measurements over a western United States natural gas field. *Geophys. Res. Lett.* **40**, 4393–4397 (2013).
- de Gouw, J. A., Parrish, D. D., Frost, G. J. & Trainer, M. Reduced emissions of CO₂, NO_x, and SO₂ from U.S. power plants owing to switch from coal to natural gas with combined cycle technology. *Earth's Future* **2**, 75–82 (2014).
- Russell, A. R., Valin, L. C. & Cohen, R. C. Trends in OMI NO₂ observations over the United States: effects of emission control technology and the economic recession. *Atmos. Chem. Phys.* **12**, 12197–12209 (2012).
- Weijermars, R. Economic appraisal of shale gas plays in Continental Europe. *Appl. Energy* **106**, 100–115 (2013).
- Selley, R. C. UK shale gas: the story so far. *Mar. Pet. Geol.* **31**, 100–109 (2012).
- Chang, Y., Liu, X. & Christie, P. Emerging shale gas revolution in China. *Environ. Sci. Technol.* **46**, 12281–12282 (2012).
- US Energy Information Administration. Technically Recoverable Shale Oil and Shale Gas Resources: An Assessment of 137 Shale Formations in 41 Countries Outside the United States. *Analysis and Projections* <http://www.eia.gov/analysis/studies/worldshalegas/> (2013).

Acknowledgements The Uintah Basin Winter Ozone Studies were a joint project led and coordinated by the Utah Department of Environmental Quality (UDEQ) and supported by the Uintah Impact Mitigation Special Service District (UIMSSD), the Bureau of Land Management (BLM), the Environmental Protection Agency (EPA) and Utah State University. This work was funded in part by the Western Energy Alliance, and NOAA's Atmospheric Chemistry, Climate and Carbon Cycle programme. We thank Questar Energy Products for site preparation and support. Funding for the 2012 LP-DOAS HNO₂ measurements was provided by the National Science Foundation (award no. 1212666). S.M.M. acknowledges the National Science Foundation for award no. 1215926. We would like to thank L. Lee and R. Cohen of UC Berkeley for their contributions and discussions relating to the representation of alkyl nitrate chemistry in this study.

Author Contributions All authors contributed to the collection of observations or the development of models for the UBWOS campaigns. P.M.E. conducted all of the modelling work using the Master Chemical Mechanism. P.M.E. and S.S.B. wrote the paper with input from all co-authors, especially J.M.R., J.A.deG. and D.D.P.

Author Information Reprints and permissions information is available at www.nature.com/reprints. The authors declare no competing financial interests. Readers are welcome to comment on the online version of the paper. Correspondence and requests for materials should be addressed to S.S.B. (steven.s.brown@noaa.gov).

METHODS

Model chemistry scheme and constraints. The meteorologically stagnant conditions associated with winter O₃ events are amenable to treatment with a box model, in which the relevant chemical reactions are simulated in a zero-dimensional 'box', which includes emissions of primary pollutants into the box and the representation of both the transport of species out of the box and dry deposition processes through a first-order physical loss term. This approach has the advantage of allowing detailed treatment of the VOC oxidation chemistry, at the expense of a comprehensive representation of dynamical processes. The approach has been applied previously⁹ to simulate winter O₃ events in the Upper Green River Basin (UGRB) of Wyoming. Our model builds upon this prior analysis in a number of respects. First, our simulation uses an explicit, rather than lumped, VOC degradation scheme. The explicit chemistry accurately simulates radical sources derived from carbonyl photolysis, key to understanding the VOC and NO_x sensitivities of O₃ production. Second, we simulate a multi-day build-up event rather than single-day ozone events. Third, our simulations use continuous emissions of VOC and NO_x, tuned to match observed levels, while the UGRB simulations used an initial VOC and NO_x concentration for each day, which was subsequently allowed to oxidize away. Fourth, our simulations use an explicit scheme for the diurnal variation in boundary-layer height (expressed as a dilution term in the box model) matched to LIDAR observations and to the diurnal variation in long-lived species, such as methane. The UGRB simulations used either a fixed boundary layer, or a linear growth in boundary layer. Fifth, our simulations are constrained to realistic diurnal variations of nitrous acid, HNO₂, based on observations, rather than expressing HNO₂ as a fixed ratio to NO₂. Sixth, our simulations appear to use a more realistic range of NO_x (<10 p.p.b.v. range for the diurnal average, rather than an initial concentration exceeding 100 p.p.b.v.). Seventh, our simulation is tested against observations of photochemical products other than ozone, such as peroxyacetyl nitrates and oxygenated VOCs, to lend confidence to the result. Lastly, our simulations explicitly calculate radical sources and their magnitude, and use this information to define the VOC and NO_x sensitivity.

Model simulations were performed using the Dynamically Simple Model of Atmospheric Chemical Complexity^{32–34} (DSMACC). The model chemistry scheme is generated by the Master Chemical Mechanism (MCM) v3.2^{18,35} and contains detailed inorganic chemistry and a near-explicit degradation scheme for 32 of the observed VOCs and OVOCs (Extended Data Table 1), resulting in 2,754 species and 10,675 reactions. The MCM v3.2 chemistry scheme has been updated to include temperature-dependent yields for organic nitrates based on ref. 36. This change to the mechanism was important because temperatures during winter ozone events are significantly lower than during more typical, summertime urban ozone formation (for example, –8.5 °C was the average during the 2013 measurements in the Uintah Basin, Utah).

The UBWOS field intensives made an extensive set of meteorological and chemical observations with which to constrain the model, including more than 60 speciated VOCs, speciated reactive nitrogen (NO_x and its major oxidation products) and photochemical radical precursors (Extended Data Table 1). Modelling of UBWOS 2012, during which there was no snow on the ground and ozone did not exceed the US national ambient air quality standards, has already been reported¹⁶. During UBWOS 2012, the deployed instrumentation provided a more extensive suite of observed VOCs than was available during 2013 (see Methods section on chemical and radiation measurements). Thus, to maximize the model constraints for UBWOS 2013, several of the UBWOS 2012 observations have been used to inform the 2013 model study. Aromatic VOCs in 2013 were measured by PTR–MS, providing a sum of all aromatic species at individual carbon numbers (that is, ΣC₉ aromatics, ΣC₁₀ aromatics and so on). The use of a GC–MS co-located with the PTR–MS in 2012 allowed the speciation of these aromatic classes. Although no GC–MS was present during UBWOS 2013, the PTR–MS aromatic classes have been allocated to specific compounds on the basis of the 2012 speciation ratios. This approach rests on the assumption that relative emissions from the oil and gas production source did not change between the two years. A similar approach was also used for the substituted cyclo-alkane species that were measured during UBWOS 2012 but not 2013. During UBWOS 2012, all the cyclo-alkanes had a similar daily profile, indicating a common source. Although many of these compounds were not measured during UBWOS 2013, their concentrations have been estimated on the basis of their observed ratio to cyclohexane in 2012. As the MCM does not contain explicit oxidation schemes for the seven substituted cyclo-alkanes whose concentrations have been estimated, these compounds have been lumped as cyclohexane for the simulations described here. The MCM chemistry scheme has also been modified to include the photolysis of ClNO₂ to yield a chlorine radical¹⁶.

All primary VOC species in the model are introduced via a constant emission over the entire six-day period, tuned to best match the observed concentrations. As the production mechanisms of HNO₂ and ClNO₂ involve uncertain heterogeneous processes, and are therefore difficult to represent in this purely gas-phase mechanism,

the concentrations of these radical precursor species have been constrained to an average diurnal concentration profile (Extended Data Fig. 1). ClNO₂ concentrations were constrained to the observed 2013 average diurnal, while HNO₂ concentrations were constrained to the observed 2012 average diurnal to provide an upper limit for its importance as a primary radical source (see Methods section on wintertime photochemistry).

NO_x within the model was constrained via a constant emission of NO. The model chemistry scheme calculates the partitioning between all reactive nitrogen compounds, and the emission of NO was adjusted to minimize the deviation between the model and observed NO_x concentration (Extended Data Fig. 1).

Data from the 2013 Uintah Basin Winter Ozone Studies are available at <http://esrl.noaa.gov/csd/groups/csd7/measurements/2013ubwos/>. National O₃ data, such as those in Fig. 1, are available from the US Environmental Protection Agency on request (<http://www.airnowtech.org>).

Photolysis rates in the model. Direct observations of $j(\text{O}^1\text{D})$ and $j(\text{NO}_2)$ were available for UBWOS 2012, but not for UBWOS 2013. Instead, a total downwelling radiation measurement was used to calculate these photolysis frequencies by comparison with data from 2012, when the total downwelling radiation measurement was run alongside calibrated filter radiometers for $j(\text{O}^1\text{D})$ and $j(\text{NO}_2)$. Polynomial fits to the data on total radiation versus filter radiometer were used to extract a calibration for the total radiation measurement for both $j(\text{O}^1\text{D})$ and $j(\text{NO}_2)$. Extended Data Fig. 2a, b shows the 2012 average diurnal $j(\text{NO}_2)$ and $j(\text{O}^1\text{D})$ filter radiometer observations and the calculated photolysis frequencies using the 2012 total radiation measurement. Photolysis frequencies for UBWOS 2013 were then calculated using the 2012 calibration for the 2013 total radiation observations (Extended Data Fig. 2a, b). The model uses the TUV radiation model³⁷ to calculate photolysis frequencies. TUV photolysis frequencies were calculated using the average observed surface albedo of 0.85 and an average observed O₃ column density of 323 Dobson units (average OMI data during observation period). The TUV calculated photolysis frequencies were then scaled to the average $j(\text{O}^1\text{D})$ and $j(\text{NO}_2)$ determined as described above, with the ratio between the measured and calculated $j(\text{NO}_2)$ being applied to all calculated photolysis rates other than $j(\text{O}^1\text{D})$.

Physical loss within the model. Observed concentrations of long-lived species, such as methane, did not continue to rise during the entirety of the six-day stagnation event, but instead accumulated during the first days of the event (approximately four days for methane; Extended Data Fig. 3a) and then levelled off. As the lifetime of methane with respect to chemical loss is of the order of years, this establishment of a steady-state concentration indicates losses due to physical mixing out of the shallow inversion layer. In addition to the multi-day trend in methane, the observed concentrations also show a diurnal pattern, with increasing concentrations until late morning and then a decrease until late afternoon. This diurnal pattern indicates increased mixing and dilution of species in the afternoon. This is consistent with LIDAR and tether sonde observations¹⁰ of boundary-layer height, which showed a growth in mixing height from 5–25 m during the night to 130–160 m between 12:00 and 16:00 local time, owing to turbulent convective mixing, before reducing again as the sun set.

A first-order loss parameter was used to represent all non-chemical loss of species through mixing, and to a lesser extent deposition, in order to prevent the accumulation of unconstrained species within the model. To represent turbulent convective mixing in this zero-dimensional model framework, a bi-modal, first-order physical loss parameter was used, with one physical loss rate used for the night and morning and a second, greater, loss rate used during the afternoon (Extended Data Fig. 3b). This parameter was adjusted to best reproduce the methane observations, and then applied to all other species within the model, after correcting for methane mixing into a non-zero (1.8 p.p.m.v.) background. The same dilution term was applied to ozone after accounting for mixing into a background of 50 p.p.b.v. (estimated using ozone LIDAR observations).

LIDAR and tether sonde observations do show some day-to-day variability in the timing and magnitude of the change in boundary-layer depth, and, thus, in dilution of the surface layer. The simple approach to representing mixing is invariant from one day to the next, and thus will not capture day-to-day changes in ozone that are due to physical losses. The simulation is intended to accurately simulate the average daily ozone response and, thus, the sensitivity to average emissions of VOCs and NO_x. Simulations where the physical loss parameter was increased or decreased by a factor of two showed changes in maximum day-six O₃ mixing ratios of –43% and +36%, respectively. These changes are due to a combination of changes in O₃ precursor concentrations within the model as well as the change in the rate of physical removal of O₃ itself. In an attempt to isolate these effects, simulations where the physical loss rate of O₃ was kept constant and that for all other species was increased or decreased by a factor of two gave changes of –20% and +8% respectively. As the relative emissions of NO_x and VOCs do not change across these simulations, it is interesting to note that the calculated daily O₃ increase on day six does not see as large a change as the absolute mixing ratio does between the base

model simulation ($\Delta[\text{O}_3] = 39$ p.p.b.v.) and the simulations with the physical loss rate for all species (including for O_3) doubled ($\Delta[\text{O}_3] = 37$ p.p.b.v.) and halved ($\Delta[\text{O}_3] = 36$ p.p.b.v.).

Ozone surface uptake rates were measured during UBWOS 2013 by eddy covariance. The determined 24 h median observed ozone deposition rate of 0.02 cm s^{-1} was included in all model simulations. This value is within the range from literature studies of $0\text{--}0.2 \text{ cm s}^{-1}$ over snow³⁸. Although included for completeness, this loss for ozone is insignificant compared with dilution and chemical losses.

LIDAR and balloon soundings from Horsepool show that the high O_3 is concentrated in the lowest few hundred metres above the surface and is not transported to the site from the free troposphere or lower stratosphere.

The model was initialized using the observed VOC, NO_x and O_3 concentrations at 00:00, 31 January 2013, and calculated oxidation product concentrations after a 24 h spin-up period from this time. The model was integrated forwards, with an output time step of 600 s, for a period of six days.

Model performance. In addition to reproducing the observed build-up of ozone over the six-day period, the model also reproduced the build-up of other photochemical oxidation products. Extended Data Fig. 4 shows the model to measurement comparisons for (a) acetaldehyde, (b) acetone, (c) 2-butanone (MEK), (d) acetyl peroxyxynitrate (PAN) and (e) propionyl peroxyxynitrate (PPN). Considering the simple dynamical representation and the calculated photolysis frequencies, the agreement between the calculated and observed oxidation products over the six-day model is excellent (with average model deviations of -2% acetaldehyde, $+44\%$ MEK, $+1\%$ PAN and -16% PPN). This agreement, calculated as the peak of a Gaussian fit to the probability distribution of the 10 min-averaged model-to-measurement deviation (Extended Data Fig. 4), gives confidence in the model's ability to reproduce the observed ozone production photochemistry.

Chemical and radiation measurements during UBWOS 2013. Data used as model inputs have been described in the preceding sections. Extended Data Table 2 summarizes the chemical and physical measurements at the Horsepool site during January and February 2013 that were used for the model analysis. For a discussion of the UBWOS 2012 measurements, we refer the reader to ref. 16.

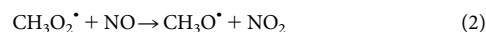
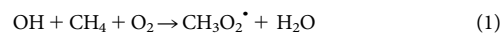
Briefly, nitrogen oxides ($\text{NO}_x = \text{NO} + \text{NO}_2$), ozone (O_3) and total reactive nitrogen (NO_y) were measured by cavity ring-down spectroscopy (CRDS) at 405 nm, which detects NO_2 directly and other species simultaneously via conversion to NO_2 (refs 39, 40). Similarly, night-time nitrogen oxides were measured by CRDS at 662 nm, detecting NO_3 directly and N_2O_5 via thermal conversion to NO_3 (ref. 41). Nitryl chloride (ClNO_2) was measured, together with speciated PANs, using chemical ionization mass spectrometry (CIMS) with iodide (I^-) as a reagent ion⁴². Potential interference due to peroxyacids was checked and found to contribute $<2\%$ to measured concentrations⁴³. Inorganic acids, including HCl, HNO_2 and HNO_3 , were measured using negative-ion proton transfer reaction (PTR) CIMS with acetate (CH_3CO_2^-) reagent ion⁴⁴. Oxygenated and aromatic VOCs were measured by PTR-MS⁴⁵ and PTR-Tof-MS⁴⁶ (Tof, time of flight) using H_3O^+ primary ions. Speciated VOCs, including alkanes, alkenes, cycloalkanes, aromatics and oxygenates were measured by GC-MS in 2012, and by GC-FID (FID, flame ionization detection) in 2013⁴⁷. Formaldehyde was measured by differential optical absorption spectroscopy⁴⁸ (DOAS) in 2012 and with PTR-MS in 2012 and 2013 using the method in ref. 49. Methane was measured using a commercial cavity ring-down instrument²⁵. Downwelling radiation was measured using a spectral pyranometer⁵⁰ as described above.

Construction of the ozone isopleth (Fig. 3). For this work to have the maximum possible relevance for policy makers, the O_3 isopleth diagram was constructed in emissions space. For this purpose, 107 model simulations were carried out across a landscape from VOC and NO_x emissions at 10% of those required to reproduce the observations in the base model to a doubling of emissions. VOC emissions were treated as a whole, with the changes applied to the emissions of all VOC species for each simulation. A contour plot was then constructed to map out the impact of these changes in NO_x and VOC emissions on the maximum calculated O_3 mixing ratio on day six of the simulation. Owing to the nonlinear nature of the chemistry, and, hence, the impact of changing emissions on absolute concentration, Fig. 3b was included to illustrate these sensitivities in VOC and NO_x concentration space.

Description of the Uintah Basin. Figure 1 shows O_3 at Ouray, Utah during 2013, and Fig. 2 shows O_3 during a six-day period in January–February at the Horsepool intensive field site. Figure 1 shows a digital elevation map of the Uintah Basin indicating the location of the Ouray and Horsepool sites and the distribution of the $\sim 11,000$ oil and gas wells. Also shown are O_3 monitors (not for regulatory purposes) deployed during the 2010–2011 winter. All fourteen monitors within the basin itself (excluding two at the far west and southwest edges of the map domain) recorded at least one, and as many as 25, days above the 75 p.p.b.v. 8 h-average US national ambient air quality standard for O_3 during this winter. Thus, these events are widespread, impacting the largest population centres (Vernal, Utah and Rangely, Colorado) in the basin⁵¹.

Sources of radicals for wintertime photochemistry. Figure 2 shows the relative contributions of different radical sources to the model simulation on day six. Extended Data Table 3 shows the absolute and relative contributions of these different radical sources.

Primary radicals versus radical amplification reactions. Understanding the source of radicals that drive tropospheric oxidation is central to understanding tropospheric O_3 photochemistry²³. Throughout the troposphere, the major primary radical source is the photolysis of O_3 and the subsequent reaction of $\text{O}(^1\text{D})$ with water vapour to yield $2 \times \text{OH}$ (ref. 15), a process that generates radicals from stable precursors without radical loss. In polluted environments, numerous other radical sources, often derived from heterogeneous reactions of NO_x or from intermediates in the VOC degradation process may also contribute^{19,52}. During UBWOS 2013, the net primary radical source was small (2.8 p.p.b.v. d^{-1} ; Fig. 2); however, the number of radicals produced by these primary sources was greatly amplified through the production of photolabile oxygenated VOCs (OVOCs), particularly carbonyl compounds, which photolyse to produce additional radicals. The simplest example of this process is the high- NO_x oxidation of methane (reactions SR1–SR5, shown in equations (1)–(5)), in which an OH attacks methane in SR1 to produce a peroxy radical. This radical is propagated through SR2, in the formation of an alkoxy radical, and SR3, in the formation of a hydro-peroxy radical, to reform OH in SR5. In addition to a hydro-peroxy radical, SR3 also produces formaldehyde, a chemically stable product of the radical propagation chain that photolyses readily (for example, during UBWOS 2013 the HCHO lifetime with respect to photolysis was approximately 4 h between the hours of 10:00 and 15:00 local time). Its photolysis produces two hydro-peroxy radicals in its dominant photolysis channel, whose yield is approximately 70% (ref. 53). Formation of two radicals in addition to the radical that is propagated through this mechanism amplifies the primary radical source



Extended Data Fig. 5a is a detailed version of the radical source pie chart shown in Fig. 2, providing a greater breakdown of the moiety of the species that constitute the carbonyl radical source. The high yield of photolabile oxygenated products (the two most significant being formaldehyde and methyl-glyoxal) in the UBWOS 2013 calculations has the effect of rapidly amplifying the primary radical production, by as much as a factor of 3–4 between the hours of 10:00 and 18:00. Formaldehyde is the single largest contributor to this source. It arises from the oxidation of all the VOCs, but, in particular, from light alkanes, such as C_2H_6 , $i\text{-C}_5\text{H}_{12}$, $i\text{-C}_4\text{H}_{10}$ and 3-methylpentane, which were highly abundant in the Uintah Basin. Oxidation of aromatics, in particular toluene and the xylenes, also produces numerous photolabile carbonyl compounds, many with both a ketone and an aldehyde functional group, including methyl-glyoxal, which is the second largest single contributor to radical production after formaldehyde in the model. A sensitivity test, in which all aromatic emissions were replaced with a cyclohexane emission sufficient to produce constant OH reactivity, leads to a 7.5% reduction in peak O_3 on day six of the simulation, demonstrating the importance of radicals derived from aromatic VOCs. The mono-aldehyde contribution to the radical source is dominated by the photolysis of acetaldehyde, propanal and isobutanol.

The high rate of VOC oxidation by OH during UBWOS 2013 was due to the large peroxy radical source, from these radical amplification processes, combined with optimal NO_x concentrations. During sunlight hours, an average of 89% of the model HO_2 reacts with NO to yield OH (after correcting for the instantaneous cycling of HO_2 with HO_2NO_2 , which is a radical reservoir, not a net sink). This fraction reaches $>98\%$ during the peak O_3 production period. As every NO-to- NO_2 conversion (by reactions other than with O_3) produces an O_3 , this efficient cycling of radicals by the available NO_x results in highly efficient O_3 production. Thus, total VOC oxidation is rapid despite moderate peak OH concentrations ($\sim 1.2 \times 10^6$ molecules cm^{-3} on day six of the simulation) due to the short OH lifetime (20–30 ms). The extremely high primary VOC concentrations in the Uintah Basin also result in OH reactions being dominated by these species rather than reaction with secondary oxidation products. This limits the reactive loss of the photolabile oxidation products, such as methyl-glyoxal, thus increasing the loss of these compounds via photolysis and increasing their dominance as the major radical source. Three-dimensional model analyses, required to better understand the physical processes

that lead to stagnation events and describe the distribution of O₃, will need to reproduce these radical sources if they are to accurately simulate photochemical O₃.

The rapid reaction of OH with VOCs and HO₂ with NO results in the dominant radical sinks being via organic peroxy radicals (Extended Data Fig. 5b). The small contribution of OH reactions to the total radical sink is indicative of the efficient VOC oxidation, and, thus, O₃ production, by OH within the model.

Nitrous acid (HNO₂). Numerous recent studies have found photolysis of HNO₂ to be a significant primary source of OH radicals, particularly in polluted (high-NO_x) environments^{22,48,52,54–60}. It is also a potentially important radical source during periods of cold or snow cover. The emission of HNO₂ from the ground or snow pack has been known for some time and has been measured as part of snow chemistry studies in Arctic, Antarctic and mid-latitude environments^{12,61–63}. One of these studies reports HNO₂ emissions from the snow pack in Wyoming during high-O₃ episodes in 2011¹². HNO₂ observations during UBWOS 2013 were made with a relatively new technique (acetate ion CIMS⁴⁴) that was suspected to suffer from chemical interference from peroxyacetic acid (HO₂NO₂), a species modelled to have been present at part-per-billion levels during the cold and photochemically active winter of 2013. Data from the CIMS were thus not used to estimate the contribution of HNO₂ to primary radical generation for the 2013 study. Measurements of HNO₂ were made during the 2012 study by both CIMS and a long-path differential optical absorption spectroscopy⁴⁸ (LP-DOAS) instrument. As noted above, the 2012 study year was characterized by warmer temperatures, no snow cover and no O₃ events above the US national ambient air quality standard¹⁶. Interference from HO₂NO₂ in the CIMS instrument under these conditions would be expected to be much smaller. The DOAS instrument was unavailable during the 2013 study, but was present in 2014, a year with snow cover but fewer O₃ exceedance events relative to 2013. Extended Data Fig. 6a shows the comparison of the diurnally averaged HNO₂ from the DOAS instrument during 2012 and 2014, along with the CIMS measurement from 2012. The CIMS HNO₂ was on average 0.032 p.p.b.v. lower than the DOAS HNO₂ in 2012, although this difference is within the 0.035 p.p.b.v. error in the DOAS HNO₂ determinations. The DOAS HNO₂ was remarkably similar between 2012 and 2014, suggesting that the presence of snow cover or active photochemistry had little influence on the mixing ratio of HNO₂. Thus, in the absence of an interference-free HNO₂ measurement during 2013, we used the daily average of the CIMS instrument from 2012 in the base-model simulation. The integrated OH radical production from the 2012 CIMS HNO₂ was 1.6 p.p.b.v. d⁻¹, compared with 2.5 and 2.6 p.p.b.v. d⁻¹ using the 2012 and 2014 DOAS data, respectively. Figure 2 in the main text shows the sensitivity of modelled O₃ to variation of HNO₂ from zero to twice the base-case model. Because all estimates for the contribution of HNO₂ are relatively modest compared with net radical production in 2013, this range has little influence on the model-to-measurement comparison for O₃.

Inclusion in the model of HNO₂ at levels comparable to those suggested in ref. 12 during winter O₃ events in Wyoming produces simulated O₃ levels larger than observations by a factor of approximately two, similar to the conclusion of a separate model analysis¹². Strong vertical gradients in HNO₂ that confine large concentrations to within a few metres of the snow surface, where HNO₂ is thought to be produced heterogeneously, may reconcile different measurement results and modelled O₃ responses, but would lead to simulation results not significantly different from those shown in Fig. 2. If there were a large ground source of HNO₂ during the 2013 year, its contribution to the entire boundary layer could be estimated with a simple eddy diffusivity model. Classic turbulent diffusion theory relates the timescale of transport of a species (*t*) to a height above the ground (*σ*, the standard deviation of a Gaussian diffusion plume) with an eddy diffusivity *K_z*:

$$t = \sigma^2 / 2K_z$$

Eddy diffusivities vary with height, being roughly proportional to height in the surface layer and rising to a maximum in the middle of the mixed layer⁶⁴. Extended Data Fig. 6b shows, at left, model results for a stable boundary layer over relatively smooth snow-covered terrain⁶⁴. The *K_z* value in the model varied up to just over 10,000 cm² s⁻¹ in the middle of a shallow boundary layer of similar height to the boundary layer observed during UBWOS 2013. This range of *K_z* values is consistent with observations during flux studies at Alert NWT⁶³ and Summit, Greenland^{62,65}. Extended Data Fig. 6b shows, at right, the relative concentration profiles corresponding to the *K_z* values ranging from 500 to 10,000 cm² s⁻¹, obtained from the diffusion time and the first-order loss rate due to photolysis (*J*_{HNO₂}) according to

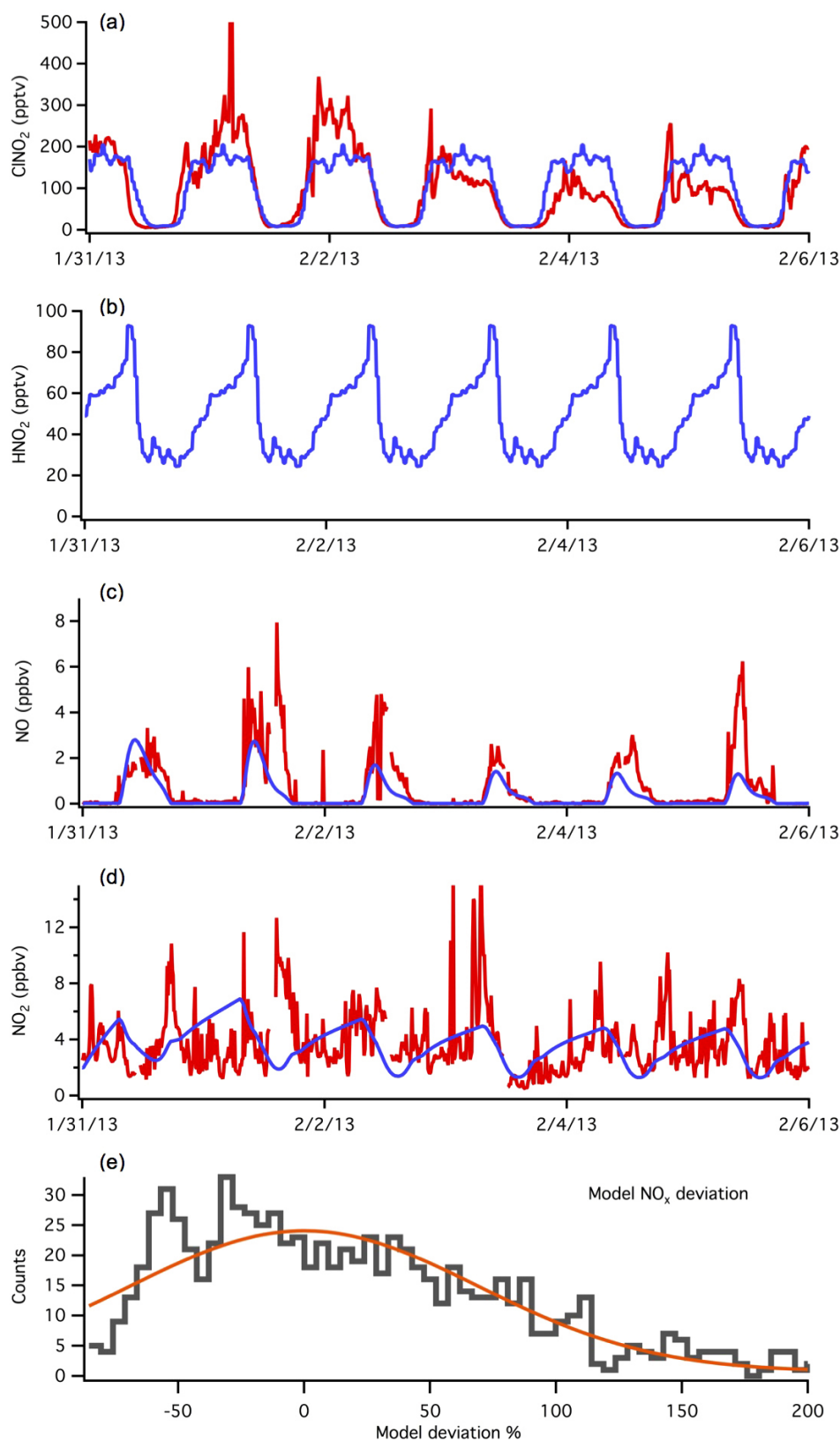
$$[\text{HNO}_2]_t / [\text{HNO}_2]_0 = \exp(-J_{\text{HNO}_2} \sigma^2 / 2K_z)$$

when the midday HNO₂ photolysis rate was 0.0016 s⁻¹ (10 min lifetime). A height profile for HNO₂ was calculated numerically from the *K_z*-vs-height results of ref. 64 and the profiles as functions of *K_z*. Under these conditions, HNO₂ decreases

rapidly with height and impacts only the lowest few tens of metres of the boundary layer. Thus, even if there were a ground source as large as that inferred in ref. 12, its contribution to radical production integrated across the entire boundary layer would be unlikely to significantly exceed that used in the simulations presented here.

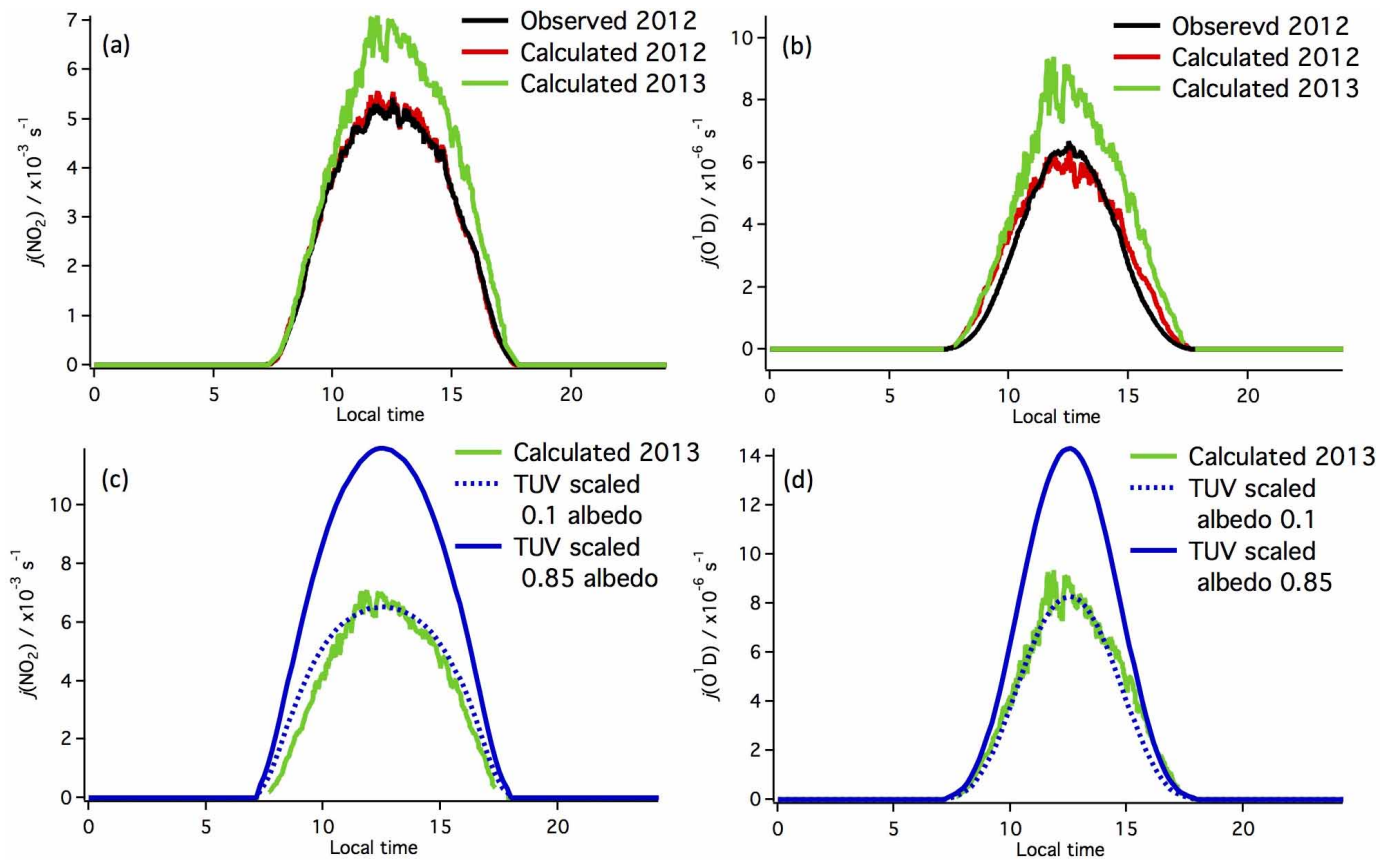
32. Edwards, P. *et al.* Hydrogen oxide photochemistry in the northern Canadian spring time boundary layer. *J. Geophys. Res.* **D 116**, D22306 (2011).
33. Emmerson, K. M. & Evans, M. J. Comparison of tropospheric gas-phase chemistry schemes for use within global models. *Atmos. Chem. Phys.* **9**, 1831–1845 (2009).
34. Stone, D. *et al.* HO_x observations over West Africa during AMMA: impact of isoprene and NO_x. *Atmos. Chem. Phys.* **10**, 9415–9429 (2010).
35. Saunders, S. M., Jenkin, M. E., Derwent, R. G. & Pilling, M. J. Protocol for the development of the Master Chemical Mechanism, MCM v3 (part A): tropospheric degradation of non-aromatic volatile organic compounds. *Atmos. Chem. Phys.* **3**, 161–180 (2003).
36. Carter, W. L. & Atkinson, R. Alkyl nitrate formation from the atmospheric photooxidation of alkanes; a revised estimation method. *J. Atmos. Chem.* **8**, 165–173 (1989).
37. Madronich, S., McKenzie, R. L., Bjorn, L. O. & Caldwell, M. M. Changes in biologically active ultraviolet radiation reaching the Earth's surface. *J. Photochem. Photobiol. B* **46**, 5–19 (1998).
38. Helmig, D., Ganzeveld, L., Butler, T. & Oltmans, S. J. The role of ozone atmosphere-snow gas exchange on polar, boundary-layer tropospheric ozone - a review and sensitivity analysis. *Atmos. Chem. Phys.* **7**, 15–30 (2007).
39. Fuchs, H. *et al.* A sensitive and versatile detector for atmospheric NO₂ and NO_x based on blue diode laser cavity ring-down spectroscopy. *Environ. Sci. Technol.* **43**, 7831–7836 (2009).
40. Washenfelder, R. A., Dubé, W. P., Wagner, N. L. & Brown, S. S. Measurement of atmospheric ozone by cavity ring-down spectroscopy. *Environ. Sci. Technol.* **45**, 2938–2944 (2011).
41. Dubé, W. P. *et al.* Aircraft instrument for simultaneous, in-situ measurements of NO₃ and N₂O₅ via cavity ring-down spectroscopy. *Rev. Sci. Instrum.* **77**, 034101 (2006).
42. Slusher, D. L., Huey, L. G., Tanner, D. J., Flocke, F. & Roberts, J. M. A thermal dissociation - chemical ionization mass spectrometry (TD-CIMS) technique for the simultaneous measurement of peroxyacetyl radicals and dinitrogen pentoxide. *J. Geophys. Res.* **109**, D19315 (2004).
43. Phillips, G. J. *et al.* Peroxyacetyl nitrate (PAN) and peroxyacetic acid (PAA) measurements by iodide chemical ionisation mass spectrometry: first analysis of results in the boreal forest and implications for the measurement of PAN fluxes. *Atmos. Chem. Phys.* **13**, 1129–1139 (2013).
44. Roberts, J. M. *et al.* Measurement of HONO, HNCO, and other inorganic acids by negative-ion proton-transfer chemical-ionization mass spectrometry (NI-PT-CIMS): application to biomass burning emissions. *Atmos. Meas. Tech.* **3**, 981–990 (2010).
45. de Gouw, J. A. *et al.* Validation of proton transfer reaction-mass spectrometry (PTR-MS) measurements of gas-phase organic compounds in the atmosphere during the New England Air Quality Study (NEAQS) in 2002. *J. Geophys. Res.* **108**, D214682 (2003).
46. Jordan, A. *et al.* A high resolution and high sensitivity proton-transfer-reaction time-of-flight mass spectrometer (PTR-TOF-MS). *Int. J. Mass Spectrom.* **286**, 122–128 (2009).
47. Kuster, W. C. *et al.* Intercomparison of volatile organic carbon measurement techniques and data at La Porte during the TexAQs 2000 air quality study. *Environ. Sci. Technol.* **38**, 221–228 (2004).
48. Wong, K. W. *et al.* Daytime HONO vertical gradients during SHARP 2009 in Houston, TX. *Atmos. Chem. Phys.* **12**, 635–652 (2012).
49. Warneke, C. *et al.* Airborne formaldehyde measurements using PTR-MS: calibration, humidity dependence, inter-comparison and initial results. *Atmos. Meas. Tech.* **4**, 2345–2358 (2011).
50. Ohmura, A. *et al.* Baseline Surface Radiation Network (BSRN/WCRP): new precision radiometry for climate research. *Bull. Am. Meteorol. Soc.* **79**, 2115–2136 (1998).
51. Martin, R. *et al.* Final Report: Uintah Basin Winter Ozone and Air Quality Study 19–24. Report No. EDL/11-039 (Utah State University, 2011).
52. Volkamer, R., Sheehy, P., Molina, L. T. & Molina, M. J. Oxidative capacity of the Mexico City atmosphere - Part 1: A radical source perspective. *Atmos. Chem. Phys.* **10**, 6969–6991 (2010).
53. Carbajo, P. G. *et al.* Ultraviolet photolysis of HCHO: absolute HCO quantum yields by direct detection of the HCO radical photoproduct. *J. Phys. Chem. A* **112**, 12437–12448 (2008).
54. Li, X. *et al.* Exploring the atmospheric chemistry of nitrous acid (HONO) at a rural site in Southern China. *Atmos. Chem. Phys.* **12**, 1497–1513 (2012).
55. Michoud, V. *et al.* Study of the unknown HONO daytime source at a European suburban site during the MEGAPOLI summer and winter field campaigns. *Atmos. Chem. Phys.* **14**, 2805–2822 (2014).
56. Oswald, R. *et al.* HONO Emissions from soil bacteria as a major source of atmospheric reactive nitrogen. *Science* **341**, 1233–1235 (2013).
57. VandenBoer, T. C. *et al.* Understanding the role of the ground surface in HONO vertical structure: high resolution vertical profiles during NACHTT-11. *J. Geophys. Res.* **118**, 10155–10171 (2013).
58. Wang, S. *et al.* Long-term observation of atmospheric nitrous acid (HONO) and its implication to local NO₂ levels in Shanghai, China. *Atmos. Environ.* **77**, 718–724 (2013).

59. Wong, K. W., Oh, H. J., Lefer, B. L., Rappenglück, B. & Stutz, J. Vertical profiles of nitrous acid in the nocturnal urban atmosphere of Houston, TX. *Atmos. Chem. Phys.* **11**, 3595–3609 (2011).
60. Zhou, X. *et al.* Nitric acid photolysis on forest canopy surface as a source for tropospheric nitrous acid. *Nature Geosci.* **4**, 440–443 (2011).
61. Beine, H. *et al.* HONO emissions from snow surfaces. *Environ. Res. Lett.* **3**, 045005 (2008).
62. Honrath, R. E. *et al.* Vertical fluxes of NO_x , HONO, and HNO_3 above the snowpack at Summit, Greenland. *Atmos. Environ.* **36**, 2629–2640 (2002).
63. Zhou, X. *et al.* Snowpack photochemical production of HONO: A major source of OH in the Arctic boundary layer in springtime. *Geophys. Res. Lett.* **28**, 4087–4090 (2001).
64. Anderson, P. S. & Neff, W. D. Boundary layer physics over snow and ice. *Atmos. Chem. Phys.* **8**, 3563–3582 (2008).
65. Jacobi, H.-W. *et al.* Measurements of hydrogen peroxide and formaldehyde exchange between the atmosphere and surface snow at Summit, Greenland. *Atmos. Environ.* **36**, 2619–2628 (2002).



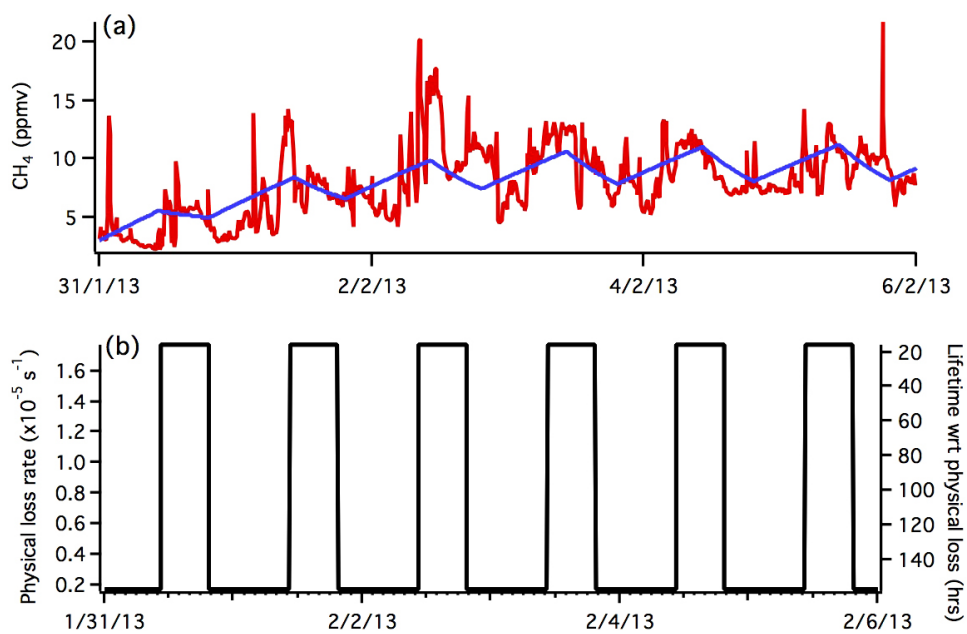
Extended Data Figure 1 | Model constraints on NO_x and radical precursors derived from NO_x. **a**, CINO₂ observations (red) and model treatment (blue). **b**, UBWOS 2012 HNO₂ average diurnal observations used to constrain model HNO₂. **c**, **d**, NO (**c**) and NO₂ (**d**) observations (red) and model values (blue) using fixed NO emission into the model and the nitrogen partitioning calculated by the chemistry scheme. The data for primary emissions (for example NO_x or CH₄) are subject to large variation owing to the influence of

local sources that produce large, transient spikes. The model, which has the continuous emission characteristic of the basin-wide total, does not capture the transients but does capture the average. This average agreement for total NO_x can be seen in the histogram of model deviation (**e**). This illustrates the frequency of model percentage deviation (grey) between each model and observation data point (both on a 10 min average). The orange fit line is a Gaussian fit to this data, centred on 0% deviation.



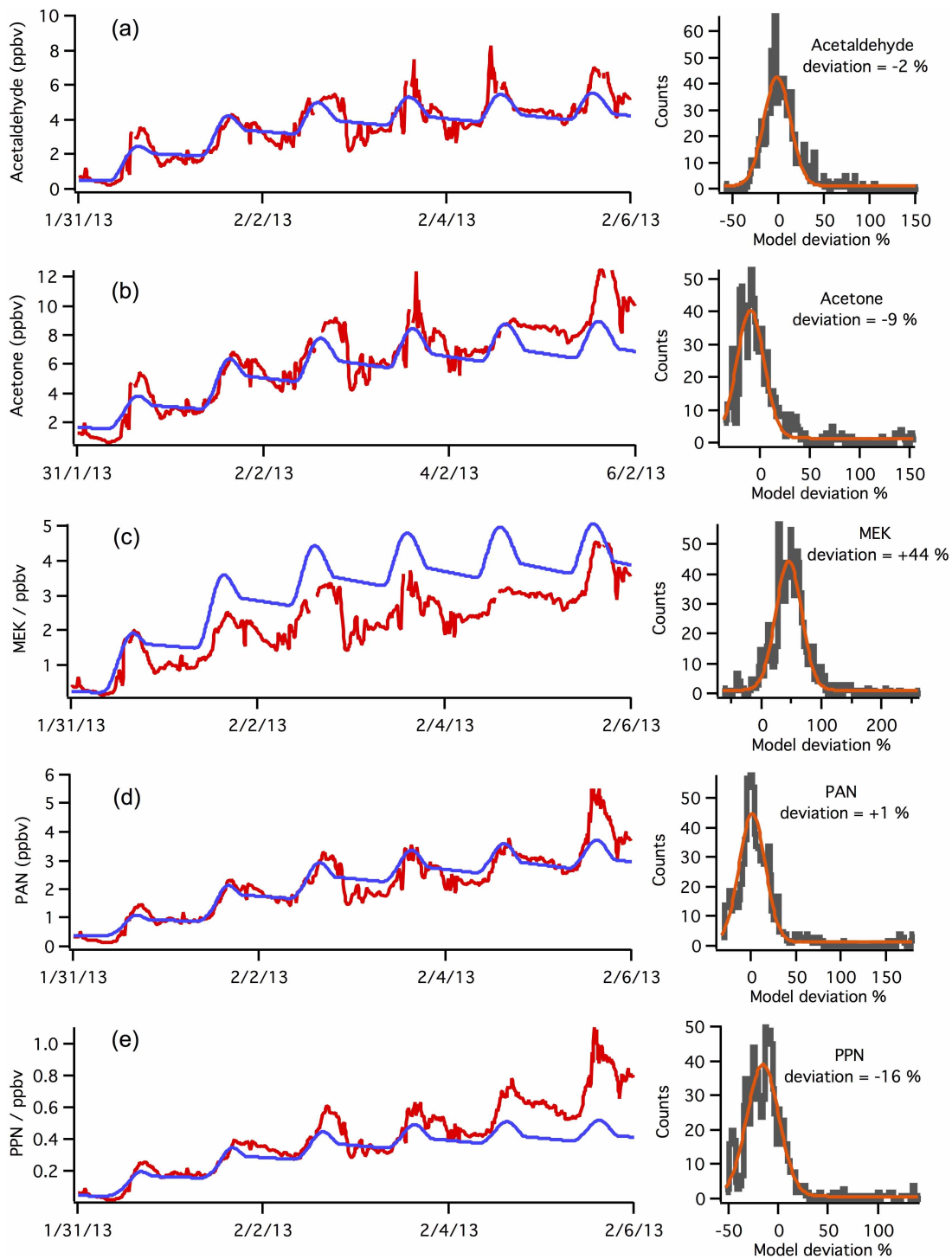
Extended Data Figure 2 | Derivation of photolysis rates from pyranometer data in 2013. a, b, Observed $j(\text{NO}_2)$ (a) and $j(\text{O}^1\text{D})$ (b) measured via filter radiometer (black) during UBWOS 2012, with calculated photolysis frequencies, using a total downwelling radiation measurement, for UBWOS

2012 (red) and UBWOS 2013 (green). c, d, TUV-calculated $j(\text{NO}_2)$ (c) and $j(\text{O}^1\text{D})$ (d) for a surface albedo of 0.1 (purely downwelling radiation; dashed blue) and for a surface albedo of 0.85 (solid blue).



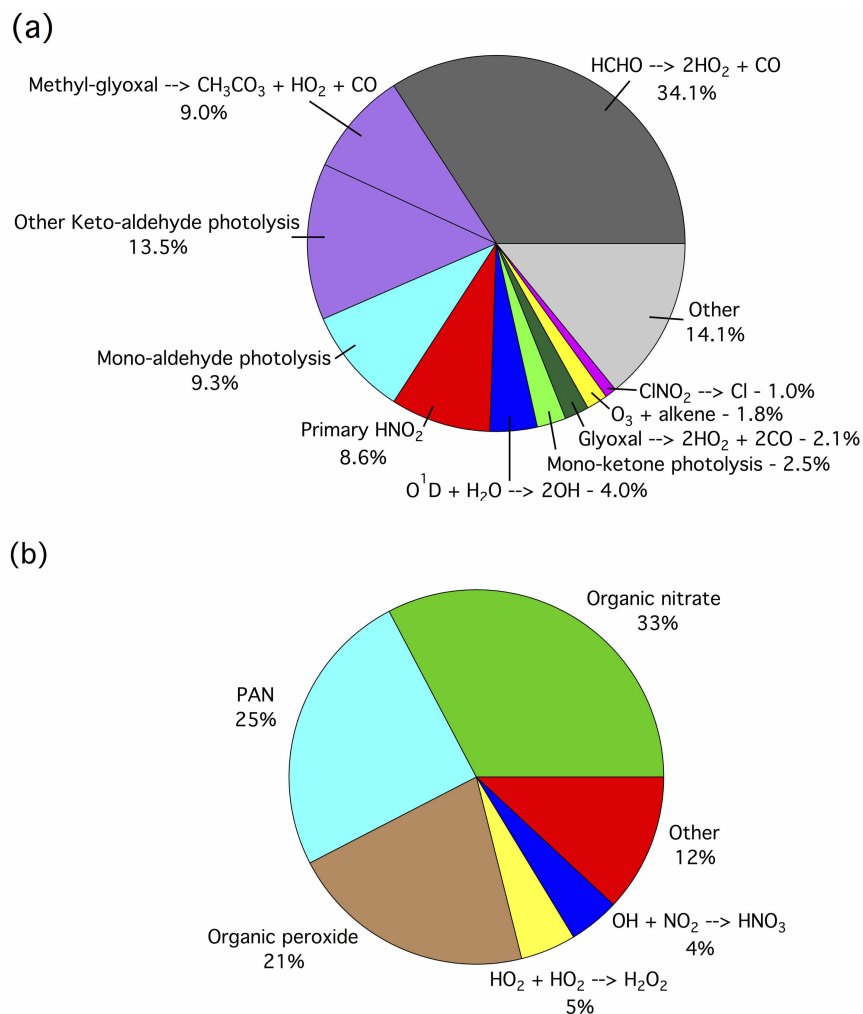
Extended Data Figure 3 | Diurnal model dilution scheme. **a**, Observed methane (red) and model values (blue) calculated using a fixed methane emission and a bimodal first-order loss process to represent dilution during the afternoon boundary layer growth. **b**, The bimodal loss parameter used to

describe all physical loss processes within the model, shown as a first-order reaction rate constant on the left axis, and a lifetime with respect to this process on the right.

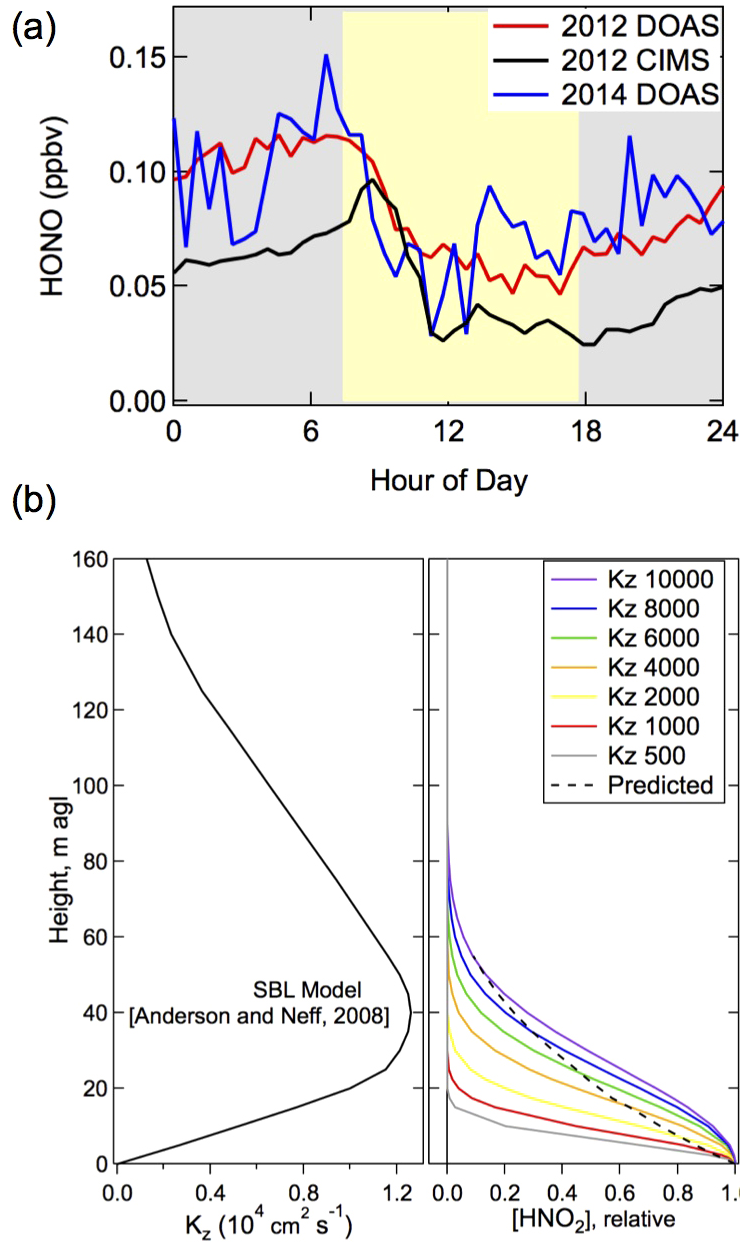


Extended Data Figure 4 | Observed (red) and model calculated (blue) mixing ratios for the oxidation products acetaldehyde (a), acetone (b), MEK (c), PAN (d) and PPN (e). The histograms show the relative model deviations

(in %) for the entire six-day simulation (grey) for the oxidation products. Gaussian fits to these probability distributions (orange) are used to describe the model skill, with the quoted deviation statistic being the peak of this fit.



Extended Data Figure 5 | Detailed radical sources and losses. **a**, Radical source contributions for day six in the model simulation. The carbonyl radical sources are separated by carbonyl moiety. **b**, Radical loss mechanisms on day six within the model.



Extended Data Figure 6 | Nitrous acid diurnal profiles and potential vertical gradients. **a**, Diurnally averaged HNO_2 mixing ratios from the 2012 (DOAS and CIMS) and 2014 (DOAS) studies. Grey and yellow shaded regions represent average durations of night and day, respectively. **b**, Left: modelled

eddy diffusivity (x axis) as a function of height above ground level; right: HNO_2 , normalized to its concentration at the surface, as a function of height above ground level for a series of eddy diffusivities. The black dashed line corresponds to the left-hand graph.

Extended Data Table 1 | Observed species used to inform the box model analysis of the ozone photochemistry during UBWOS 2013

Observed species	Model treatment	Observational technique
1,2,3-Trimethylbenzene	Constant emission	PTR-MS with speciation from 2012 GC-MS
1,2,4-Trimethylbenzene	Constant emission	PTR-MS with speciation from 2012 GC-MS
1,3,5-Trimethylbenzene	Constant emission	PTR-MS with speciation from 2012 GC-MS
2-Butanone	Model calculated	PTR-MS
2-Ethyltoluene	Constant emission	PTR-MS with speciation from 2012 GC-MS
2,2-Dimethylbutane	Constant emission	GC-FID
2,2-Dimethylpropane	Constant emission	GC-FID
3-Ethyltoluene	Constant emission	PTR-MS with speciation from 2012 GC-MS
Σ(2-, 3-Methylpentane)	Constant emission (lumped as 3-Methylpentane)	GC-FID
3,5-Diethyltoluene	Constant emission	PTR-MS with speciation from 2012 GC-MS
5-Ethyl-m-xylene	Constant emission	PTR-MS with speciation from 2012 GC-MS
Benzene	Constant emission	GC-FID
C ₂ H ₂	Constant emission	GC-FID
C ₂ H ₄	Constant emission	GC-FID
C ₂ H ₆	Constant emission	GC-FID
C ₃ H ₆	Constant emission	GC-FID
C ₃ H ₈	Constant emission	GC-FID
CH ₃ CHO	Model calculated	PTR-MS
CH ₃ OH	Model calculated + constant emission	PTR-MS
CH ₄	Constant emission	Cavity ringdown spectroscopy
CINO ₂	Constrained to 2013 observed average diurnal	∫ CIMS
CO	Fixed at 182.84 ppbv	UBWOS 2012 campaign mean
Cyclohexane	Constant emission	GC-FID + scaled UBWOS 2012 data
Ethyl-benzene	Constant emission	PTR-MS with speciation from 2012 GC-MS
HCHO	Model calculated + constant emission	PTR-MS
HNO ₂	Constrained to 2012 observed average diurnal	Acid-CIMS
<i>i</i> -C ₄ H ₁₀	Constant emission	GC-FID
<i>i</i> -C ₅ H ₁₂	Constant emission	GC-FID
Isopropylbenzene	Constant emission	PTR-MS with speciation from 2012 GC-MS
<i>m</i> -Xylene	Constant emission	PTR-MS with speciation from 2012 GC-MS
<i>n</i> -C ₄ H ₁₀	Constant emission	GC-FID
<i>n</i> -C ₅ H ₁₂	Constant emission	GC-FID
<i>n</i> -C ₆ H ₁₄	Constant emission	GC-FID
<i>n</i> -C ₇ H ₁₆	Constant emission	GC-FID
NO	via NO emission	Cavity ringdown spectroscopy
NO ₂	via NO emission	Cavity ringdown spectroscopy
<i>o</i> -Xylene	Constant emission	PTR-MS with speciation from 2012 GC-MS
O ₃	Model calculated	Cavity ringdown spectroscopy
Acetyl peroxyxynitrate	Model calculated	∫ CIMS
Propionyl peroxyxynitrate	Model calculated	∫ CIMS
Propylbenzene	Constant emission	PTR-MS with speciation from 2012 GC-MS
Toluene	Constant emission	PTR-MS

Extended Data Table 2 | Chemical and radiation measurements used in this analysis for modelling of UBWOS 2013 ozone events

Species	Technique	Accuracy
NO, NO ₂ , NO _y , O ₃	CRDS	5%
NO ₃ , N ₂ O ₅	CRDS	20%
ClNO ₂	Γ CIMS	30%
CH ₂ O	PTRMC	30%
Speciated PANs	Γ CIMS	15 %
Inorganic Acids (HCl, HNO ₂ , HNO ₃)	Acetate CIMS	30%
Speciated VOC	GC-FID	20%
Speciated VOC	PTRMS	25 %
Speciated VOC	PTR-Tof-MS	25 %
CH ₄	CRDS	2 ppbv
Downwelling Radiation	Spectral Pyranometer	7%

Extended Data Table 3 | Radical sources in the MCM simulation on day six

Radical Source	Daily Production (ppbv)	% of Total
O(¹ D) + H ₂ O	0.74	4.0
ClNO ₂ Photolysis	0.18	1.0
HNO ₂ Photolysis	1.58	8.6
O ₃ + Alkene	0.34	1.8
H ₂ CO Photolysis	6.29	34.1
Other Carbonyl Photolysis	9.32	50.5